Thermomechanical Uncertainty Analysis of Steel Partition Walls Using Direct FE^2 and Polynomial Chaos Expansion

Sen Yang[1], Yanming Xu[2], Lian Huang[3] and Linchao Liu[1,*]

[1] College of Architecture and Civil Engineering, Xinyang Normal University, Xinyang, 464000, China

[2] Henan International Joint Laboratory of Structural Mechanics and Computational Simulation, College of Architecture and Civil Engineering, Huanghuai University, Zhumadian, 463000, China

[3] Solux College of Architecture and Design, University of South China, Hengyang, 421200, China

INFORMATION

Keywords:
Steel partition walls
thermo-mechanical coupling
uncertainty analysis
direct FE^2
PCE

DOI: 10.23967/j.rimni.2025.10.70008

SCIPEDIA
Revista Internacional de Métodos Numéricos para Cálculo y Diseño en Ingeniería
RIMNI

Thermomechanical Uncertainty Analysis of Steel Partition Walls Using Direct FE^2 and Polynomial Chaos Expansion

Sen Yang[1], **Yanming Xu**[2], **Lian Huang**[3] **and Linchao Liu**[1,*]

[1]College of Architecture and Civil Engineering, Xinyang Normal University, Xinyang, 464000, China

[2]Henan International Joint Laboratory of Structural Mechanics and Computational Simulation, College of Architecture and Civil Engineering, Huanghuai University, Zhumadian, 463000, China

[3]Solux College of Architecture and Design, University of South China, Hengyang, 421200, China

ABSTRACT

Steel partition walls are essential components in modern civil engineering, providing both structural support and spatial separation. These walls are frequently exposed to combined thermal and mechanical loads, particularly in specialized environments such as high-temperature workshops or fire scenarios, where their thermo-mechanical coupling behavior is critical to building safety and functionality. This study integrates the direct finite element squared (Direct FE^2) method with generalized polynomial chaos expansion (PCE) to quantify the uncertainties in key material properties-namely, the elastic modulus and the coefficient of thermal expansion-and to evaluate their effects on the thermo-mechanical performance of steel partition walls. The proposed approach enables efficient simulation of material uncertainties and their influence on structural behavior under coupled thermal-mechanical conditions. Case studies demonstrate both the accuracy and computational efficiency of the method, while sensitivity analysis highlights the most influential uncertainty factors. The integration of Direct FE^2 and PCE thus offers a robust framework for assessing the reliability of steel partition walls under uncertain conditions, providing valuable insights for design optimization and enhancing the safety and efficiency of building structures in practical applications.

OPEN ACCESS

Received: 05/07/2025

Accepted: 17/09/2025

Published: 23/01/2026

DOI
10.23967/j.rimni.2025.10.70008

Keywords:
Steel partition walls
thermo-mechanical coupling
uncertainty analysis
direct FE^2
PCE

1 Introduction

In modern civil engineering, steel partition walls are widely employed structural components that play a critical role in both dividing interior spaces and providing structural support. The design and application of these walls must satisfy not only mechanical performance requirements, but also thermal considerations in complex service environments. During practical use, steel partition walls are often subjected to combined thermal and mechanical loads, particularly in specialized settings such as high-temperature workshops or fire scenarios, where their thermo-mechanical coupling behavior is essential to ensure building safety and functionality [1]. Therefore, accurately assessing the performance of

---

*Correspondence: Linchao Liu (liulinchao7887@163.com). This is an article distributed under the terms of the Creative Commons BY-NC-SA license

steel partition walls under coupled thermomechanical conditions is crucial for architectural design, optimization, and safety evaluation.

Current research approaches for analyzing temperature distributions and thermal stresses in partition walls generally fall into three categories: numerical simulation, experimental testing, and theoretical analysis. Among numerical methods, the finite element method (FEM) [2–4], the finite difference method (FDM) [5,6], and the finite volume method (FVM) [7,8] have become mainstream tools to solve heat conduction problems. Experimental techniques utilize thermocouples, infrared thermography [9], strain gauges, and digital image correlation (DIC) [10] to empirically measure and visualize thermal responses. Theoretical analyses, based on Fourier's law of heat conduction and thermoelastic theory [11–13], provide closed-form or semi-analytical solutions under idealized assumptions, offering benchmarks for model validation and parameter sensitivity studies.

However, these approaches exhibit notable limitations. Numerical simulations often incur high computational costs when modeling fine-scale details of multilayered or heterogeneous materials, restricting their application in real-time analysis and large-scale engineering projects [14]. Experimental methods face challenges associated with sensor accuracy and environmental interference, which can compromise data repeatability and generalizability [15]. Theoretical models, typically assuming steady-state conditions, often fail to accurately capture transient processes and nonlinear heat conduction effects [16]. Furthermore, contemporary partition walls increasingly exhibit multiscale characteristics, such as porous or composite structures, to meet rising demands for enhanced thermo-mechanical performance. At the micro-scale, the steel's microstructural features (e.g., grain size and phase composition) influence material properties such as thermal conductivity, Young's modulus and the coefficient of thermal expansion. On the macro-scale, general structural design factors (e.g., wall thickness and connection methods) further affect the thermo-mechanical coupling behavior of the wall. These multiscale attributes substantially complicate the analysis of steel partition wall performance.

One potential solution to this challenge is the concurrent multiscale modeling approach, particularly the finite element squared (FE^2) method [17,18]. Originally proposed by Feyel based on Hill-Mandel homogenization theory [19,20], this method maps the macroscopic strain field to a representative volume element (RVE) and returns the homogenized stress response, allowing high-fidelity simulations of heterogeneous materials [21]. However, traditional FE^2 methods involve cross-scale iterative calculations at each Gaussian integration point, resulting in high computational costs and increased implementation complexity [22].

To overcome these limitations, Tan et al. [23] introduced the direct finite element squared (Direct FE^2) method. By integrating macro- and micro-scale models into a unified framework through periodic boundary conditions (PBCs), multi-point constraints (MPCs), and internal virtual work equivalence [24–27], this approach improves the coupling efficiency and numerical stability between the RVE and the macro finite element model [28]. Since its introduction, Direct FE^2 has been widely applied in diverse fields, including dynamic simulations of heterogeneous media, thermo-mechanical analyses of isotropic and laminated structures, and failure modeling of composites and concrete structures [29–33].

Traditional numerical methods often rely on deterministic parameters and neglect uncertainties in material properties, such as thermal conductivity, Young's modulus, and the coefficient of thermal expansion, which can substantially affect structural performance. In practice, these parameters may vary due to manufacturing processes, environmental conditions, or operational factors. For example, Young's modulus can be influenced by material aging, environmental exposure, or fabrication techniques [34], while the thermal expansion coefficient may fluctuate due to residual stresses or uneven temperature distributions [35]. Consequently, analyses based solely on deterministic parameters may produce significant discrepancies between predicted and actual structural behavior [36,37].

To more accurately capture the performance of steel partition walls under realistic service conditions, thermo-mechanical coupling analyses that account for material parameter uncertainties are essential. Classical approaches, including Monte Carlo simulations, spectral stochastic methods, and perturbation techniques [38–41], effectively characterize the statistical properties of material responses but are often computationally intensive [42,43]. Surrogate modeling has emerged as an efficient alternative, with Polynomial Chaos Expansion (PCE) being particularly promising [44]. By representing system responses as polynomial functions of random input parameters, PCE efficiently quantifies the impact of uncertainties while significantly reducing computational costs. PCE has been successfully applied in various engineering domains, including acoustics, structural mechanics, and structural-acoustic coupling problems using deep learning-based surrogate models [45,46]. However, its application to thermo-mechanical coupling in steel partition walls remains largely unexplored.

Although the integration of Direct FE^2 and PCE have previously been investigated, and studies have focused on piezoelectric materials [47], emphasizing electromechanical coupling at the material scale. To the best of our knowledge, this combined framework has not yet been applied to thermo-mechanical problems in civil engineering structures. In particular, uncertainty analysis of steel partition walls-a critical component in fire and elevated-temperature conditions-remains unaddressed. The novelty of this study lies in adapting the Direct FE^2-PCE methodology from material-scale electromechanical applications to structural-scale thermo-mechanical uncertainty analysis, thereby establishing a new connection between multiscale computational frameworks and the safety evaluation of structural steel systems.

For this study, Q335 structural steel was selected for the partition wall, as it is widely used in civil engineering applications in China, particularly in building partition systems. Its mechanical and thermal properties are well documented, making it a representative and reliable candidate for thermo-mechanical analysis. Consequently, the conclusions drawn from Q335 can generally be considered applicable to structural steel partition walls under service and moderate thermal conditions.

In this study, we combine Direct FE^2 with generalized PCE to perform an uncertainty analysis of steel partition walls under thermo-mechanical coupling conditions. This approach incorporates the randomness of key material parameters, namely the elastic modulus and the coefficient of thermal expansion, and uses the efficient numerical simulation capabilities of Direct FE^2 to quantify the impact of material uncertainties on macro-scale thermo-mechanical responses. Case studies validate the method's accuracy and computational efficiency, while sensitivity analyses identify the most influential uncertainty factors [48,49]. The results provide theoretical support and methodological guidance for the optimization and reliability assessment of steel partition wall structures.

2 Theory of Thermo-Mechanical Coupling Concurrent Multiscale Modelling

The fundamental equations describing transient thermomechanical problems encompass both thermal and mechanical fields and can generally be formulated as follows:

$$\begin{aligned} &\rho \dot{U} = -div q_i + \rho r \\ &\rho \ddot{u}_i = -div \sigma_{ij} + \rho b_i \end{aligned} \tag{1}$$

where ρ and $\dot{U} = C_p \frac{dT}{dt}$ are the density of the material and the rate of the internal energy of the material, respectively, and C_p represents the specific heat of the material. $q_i = -k_{ij} T_{,j}$ is the heat flux where k_{ij} is the thermal conductivity and represents the temperature gradient. r denotes the internal heat source per unit volume, which is set to zero in this study due to the absence of internal heat generation. $\ddot{U}$ denotes the acceleration field, σ_{ij} represents the Cauchy stress tensor, and b_i is the body force.

For finite element analysis, the thermal governing equation is typically transformed into the following weak form:

$$\int_V \rho \dot{U} \delta T dV + \int_V q_i \delta T_{,j} dV = \int_\Gamma q_\Gamma \delta T d_\Gamma \tag{2}$$

where $\rho \dot{U} \delta T$ representing the heat exchanged per unit mass during a temperature change, this heat capacity term is essential in transient thermal simulations, while it has no effect in steady-state scenarios.

Given that partition walls primarily sustain static loads, the mechanical governing equation simplifies to the following weak form, with inertia and body force terms omitted.

$$\int_V \sigma_{ij} \delta \varepsilon_{ij} dV = \int_V \left(\sigma_{ij}^M + \sigma_{ij}^T\right) \delta \varepsilon_{ij} dV = \int_\Gamma t_i \delta u_i d\Gamma \tag{3}$$

Here, the total stress tensor σ_{ij} is composed of two parts: the mechanical stress σ_{ij}^M and the thermal stress σ_{ij}^T, such that $\sigma_{ij} = \sigma_{ij}^M + \sigma_{ij}^T$. Mechanical stress is given by $\sigma_{ij}^M = C_{ijkl}\varepsilon_{kl}$, while thermal stress is defined as $\sigma_{ij}^T = -C_{ijkl}\beta_{kl}(T - T_0)$, where ε_{kl} is the mechanical strain and $(T - T_0)$ represents the change in temperature relative to a reference temperature T_0. The tensor C_{ijkl} denotes the fourth-order elastic stiffness tensor, and β_{kl} is the coefficient of thermal expansion. The displacement field is denoted by u, and the strain tensor is defined as $\varepsilon_{ij} = \frac{1}{2}(u_{i,j} + u_{j,i})$. Here, u_i represents the displacement field and t_i denotes the traction force on the boundary. The indices $i, j = 1, 2$ correspond to two-dimensional problems considered in this work.

To accurately model coupled thermomechanical behavior, it is necessary to consider Eqs. (2) and (3) simultaneously. The internal energy density is obtained by summing the contributions from the left-hand sides of both equations:

$$\delta H_{den} = \sigma_{ij} \delta \varepsilon_{ij} + \rho \dot{U} \delta T + q_i \delta T_{,i} \, . \tag{4}$$

It is worth emphasizing that the macro-scale behavior is significantly influenced by the underlying micro- and meso-scale structural characteristics. To concurrently capture both macro- and meso-scale phenomena, the Direct FE^2 approach employs a coarse finite element discretization at the macro level while assigning a RVE at each Gauss integration point within the macro-elements to characterize the meso-scale heterogeneity. An illustrative application of the Direct FE^2 framework to a fiber-reinforced composite panel is presented in Fig. 1, the RVE is defined with specified dimensions in length and width to reflect the meso-structural configuration. Variables marked with $\hat{\blacktriangle}$ are evaluated on the meso-scale, whereas all others are defined on the macro-scale. Consistently, the gradient of a meso-scale variable is denoted using $\hat{\blacktriangle}_{,i} = \dfrac{\partial \hat{\blacktriangle}}{\partial \hat{x}_i}$.

Hence, the total internal energy at the meso-scale, evaluated in terms of its volume average, can be expressed as:

$$\left\langle \delta \hat{H} \right\rangle = \frac{1}{\left|\hat{V}\right|} \int_{\hat{V}} \left(\hat{\sigma}_{ij} \delta \hat{\varepsilon}_{ij} + \hat{\rho} \dot{\hat{U}} \delta \hat{T} + q_i \delta \hat{T}_{,i} \right) d\hat{V} \tag{5}$$

where $\langle * \rangle$ denotes volume-averaged quantities, and $|\hat{V}|$ is the volume of the RVE, a small-scale material sample statistically representing the heterogeneous material in multiscale simulations.

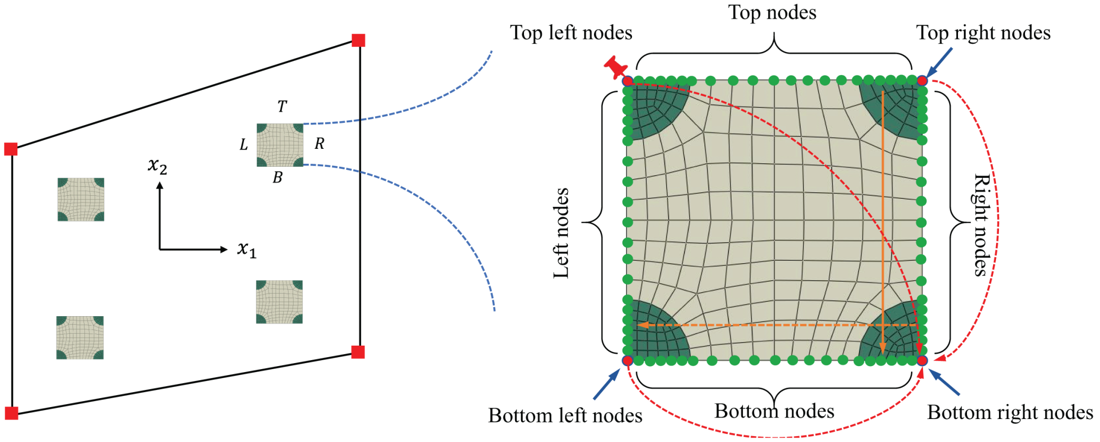

Figure 1: The schematic diagram of a Direct FE^2 model and the corresponding direct numerical simulation modeling approach

In order to enforce energetic equilibrium and satisfy kinematic coupling between the macro- and meso-scale domains, the meso-scale RVEs are subjected to periodic boundary conditions, formulated as follows (see Fig. 1):

$$\begin{aligned}
&\hat{u}_1|_{\mathrm{R}} - \hat{u}_1|_{\mathrm{L}} = 2l_1\nabla_1 u_1\\
&\hat{u}_2|_{\mathrm{R}} - \hat{u}_2|_{\mathrm{L}} = 2l_1\nabla_1 u_2\\
&\hat{T}|_{\mathrm{R}} - \hat{T}|_{\mathrm{L}} = 2l_1\nabla_1 T\\
&\hat{u}_1|_{\mathrm{T}} - \hat{u}_1|_{\mathrm{B}} = 2l_2\nabla_2 u_1\\
&\hat{u}_2|_{\mathrm{T}} - \hat{u}_2|_{\mathrm{B}} = 2l_2\nabla_2 u_2\\
&\hat{T}|_{\mathrm{T}} - \hat{T}|_{\mathrm{B}} = 2l_2\nabla_2 T
\end{aligned} \tag{6}$$

where T, L, R, B represent the RVE's top, left, right, and bottom edges.

To satisfy the Hill-Mandel macro-homogeneity condition, the meso-scale RVEs must also be scaled accordingly, leading to the following relation:

$$\tilde{w}_\alpha = \frac{w_\alpha J_\alpha}{|\hat{V}_\alpha|} = 1 \tag{7}$$

which indicates that volume $\hat{V}_\alpha$ of RVE at Gaussian point c needs to be scaled to $w_\alpha J_\alpha$. In 2D analyses, the required scaling can be conveniently applied by modifying the RVE's thickness. However, in 3D settings, the RVE undergoes uniform scaling across all three coordinate directions.

3 A Parametric Investigation Employing the Coupled Direct FE^2 and PCE Frameworks

To conduct a parametric analysis of multiscale thermo-mechanically coupled structures, it is often necessary to evaluate a large number of data samples-potentially in the thousands-to adequately capture the inherent uncertainties in material and structural properties. Despite the considerable reduction in computational cost afforded by the Direct FE^2 approach, performing such a large number of simulations remains computationally prohibitive.

To address this limitation, the Direct FE^2 method is combined with the PCE technique. PCE is a widely employed surrogate modeling approach in stochastic finite element analysis, which approximates the system response by projecting it onto a series of orthogonal polynomial basis functions defined over the probability space of input uncertainties. These polynomials are selected according to the probability distributions of the input random variables, enabling efficient uncertainty quantification without the need for exhaustive simulations.

Within the context of multiscale thermo-mechanical analysis, the PCE approach facilitates investigation of how uncertainties in meso-scale material properties affect the macroscopic thermal and mechanical behavior of heterogeneous structures. Meso-scale parameters are treated as random variables within prescribed bounds pertinent to the parametric study, allowing for the construction of an efficient and accurate surrogate model for predicting the global structural response.

In this study, the meso-scale elastic modulus $\hat{E}^m_{ijkl}$ and thermal expansion coefficient $\hat{\beta}^m_{ij}$ are treated as the only random input parameters, as they are the most influential on the thermo-mechanical response of steel partition walls under the considered moderate heating conditions. Other parameters, such as thermal conductivity and yield strength, are assumed deterministic because their variability has a relatively minor effect on the coupled response within the elastic regime. For a multiscale system containing m distinct meso-scale material types, the random input vector is defined as:

$$\mathbf{x} = \left[\hat{E}^m_{ijkl}, \hat{\beta}^m_{ij}\right]^T \tag{8}$$

The macroscopic response of interest $Y(\mathbf{x})$—which may represent temperature, heat flux, stress, or thermal strain—is approximated by a truncated PCE:

$$\Upsilon(\mathbf{x}) = \sum_{\alpha=0}^{N-1} c_\alpha \Phi_\alpha(\mathbf{x}) \tag{9}$$

where $\Phi_\alpha(\mathbf{x})$ represents a set of multivariate orthogonal polynomials constructed with respect to the distribution of the random vector $\mathbf{x}$, and c_α denotes the corresponding expansion coefficients.

The total number of polynomial terms N included in the truncated PCE model is given by the combinatorial expression:

$$N = \frac{(n+p)!}{n!\,p!} \tag{10}$$

with n being the number of uncertain input parameters and p the maximum polynomial degree in the expansion.

Multivariate orthogonal polynomials $\Phi_\alpha(\mathbf{x})$ are constructed as tensor products of corresponding univariate orthogonal polynomials:

$$\Phi_\alpha(\mathbf{x}) = \prod_{i=1}^{n} \mathit{\Phi}_{\alpha i}(x_i) \tag{11}$$

where $\mathit{\Phi}_{\alpha i}$ refers to the one-dimensional orthogonal polynomial associated with the i-th random input x_i in $\mathbf{x}$.

To determine the expansion coefficients c_α, a set of K training samples is $\left(\mathbf{x}^k, Y^k\right)$ generated using Direct FE^2 simulations. The coefficients are then obtained via least-squares fitting:

$$\boldsymbol{C} = \left(\boldsymbol{\Phi}^{\mathrm{T}}\boldsymbol{\Phi}\right)^{-1}\boldsymbol{\Phi}^{\mathrm{T}}\mathbf{U} \tag{12}$$

where $\boldsymbol{C}$ denotes the full coefficient vector c_α, and $\mathbf{U}$ corresponds to the response vector evaluated at the sample locations.

$$\boldsymbol{C} = [c_0, c_1, ..., c_{N-1}]^T, \; \mathbf{U} = \left[Y^1\left(\mathbf{x}^1\right), \; Y^2\left(\boldsymbol{x}^2\right), ..., \; Y^K\left(\mathbf{x}^K\right)\right]^T \tag{13}$$

and $\boldsymbol{\Phi}$ is a matrix $K \times N$ with the basis polynomials Φ_α evaluated at each sample point:

$$\boldsymbol{\Phi} = \begin{bmatrix} \Phi_0\left(\mathbf{x}^1\right) & \Phi_1\left(\mathbf{x}^1\right) & \ldots \Phi_{N-1}\left(\boldsymbol{x}^1\right) \\ \Phi_0\left(\mathbf{x}^2\right) & \Phi_1\left(\mathbf{x}^2\right) & \ldots \Phi_{N-1}\left(\mathbf{x}^2\right) \\ \vdots & \vdots & \vdots \\ \Phi_0\left(\mathbf{x}^K\right) & \Phi_1\left(\mathbf{x}^K\right) & \ldots \Phi_{N-1}\left(\mathbf{x}^K\right) \end{bmatrix} \tag{14}$$

Assuming that the input parameters follow a Gaussian distribution with mean μ, standard deviation σ, and coefficient of variation $COV = \frac{\sigma}{\mu}$, the corresponding univariate orthogonal basis is the Hermite polynomial. The Hermite polynomials $H_\alpha(x)$ can be expressed either in differential form:

$$H_\alpha(x) = (-1)^\alpha e^{x^2/2} \frac{d^\alpha}{dx^\alpha}\left(e^{-x^2/2}\right) = \alpha! \sum_{k=0}^{\lfloor \alpha/2 \rfloor} \frac{(-1)^k}{k!\,2^k(\alpha-2k)!} x^{\alpha-2k} \tag{15}$$

where $[\bullet]$ is defined as the floor function, and x corresponds to the set of random parameters.

The Hermite orthogonal polynomials can alternatively be generated using a recurrence relation. Fig. 2 presents the first six Hermite polynomials derived from this approach:

$$H_{\alpha+1}(x) = xH_\alpha(x) - \alpha H_{\alpha-1}(x) \tag{16}$$

To evaluate the precision of the constructed PCE surrogate model, the coefficient of variation (CV) based on the relative root mean square error (RRMSE) is used:

$$\mathrm{CV} = \frac{\sqrt{\frac{1}{N}\sum_{k=1}^{N}(Y^k - \hat{Y}^k)^2}}{\frac{1}{N}\sum_{k=1}^{N} Y^k} \tag{17}$$

The multiscale parametric study, which investigates how meso-scale material characteristics affect the overall structural behavior, can be outlined through the following steps:

1. Generate K random input samples x^k for meso-scale material parameters;
2. Perform Direct FE^2 simulations to compute macro-scale responses Y^k;
3. Construct the PCE surrogate model using the sample set;
4. Use the model to analyze the sensitivity of macro-scale responses to meso-scale variations.

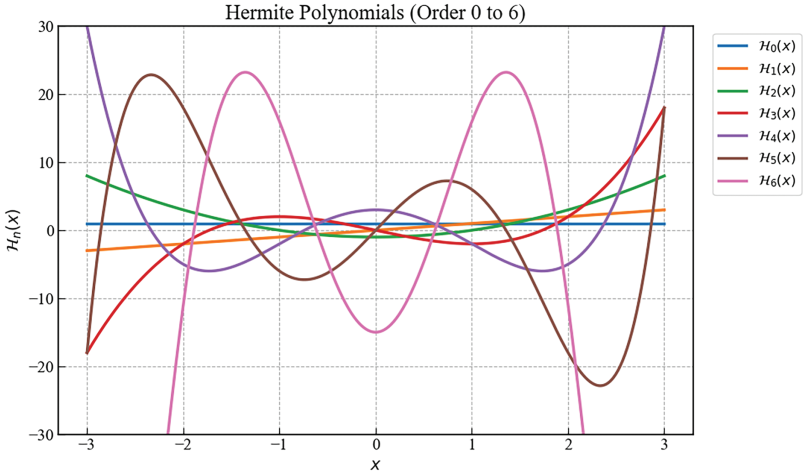

Figure 2: The first six polynomials of Hermite orthogonal polynomials

3.1 Verification and Performance Evaluation: Comparison between Direct FE^2 and DNS

To validate the accuracy and robustness of the proposed Direct FE^2 method in thermo-mechanical multiscale modeling, this section compares its simulation results with those obtained from full-scale Direct Numerical Simulation (DNS). In addition, the feasibility and computational efficiency of employing Direct FE^2 to construct a PCE surrogate model are evaluated.

The case study considers a perforated steel wall panel commonly used in building engineering to reduce self-weight. The panel geometry is defined by a length $L = 4\,\mathrm{m}$, height $H = 3\,\mathrm{m}$, and thickness $t = 20\,\mathrm{mm}$. The internal perforations are arranged periodically, with a diameter of 12.5 mm and a center-to-center spacing of 50 mm.

Regarding the boundary conditions, a vertical displacement of 20 mm is prescribed at the top edge to simulate mechanical loading. For the thermal boundary conditions, the right edge is exposed to a constant temperature of 200°C, the left edge is maintained at 20°C, and the remaining two edges are assumed adiabatic (see Fig. 3a). The maximum temperature of 200°C is selected to represent service-level or moderate heating conditions, under which steel predominantly exhibits elastic-plastic behavior without substantial thermal degradation. This choice allows the study to focus on the propagation of thermo-mechanical uncertainties under realistic operating scenarios. Although structural steel can reach temperatures above 600°C during fire events, the modeling of such extreme conditions lies beyond the scope of this work and will be addressed in future studies.

All simulations are carried out using CPS4T plane stress elements with geometric nonlinearity activated. The steel is modeled with an elastic-plastic constitutive law incorporating isotropic hardening, and the corresponding material parameters are summarized in Table 1.

In the present work, steel is modeled using an elastic-plastic constitutive relation. Nevertheless, the central objective is to elucidate the influence of parameter uncertainty on the thermo-mechanical response, rather than to provide precise predictions of plastic failure. Therefore, localized stresses that exceed the yield strength are interpreted as representative of general response tendencies, and should not be construed as an assessment of the ultimate load-bearing capacity.

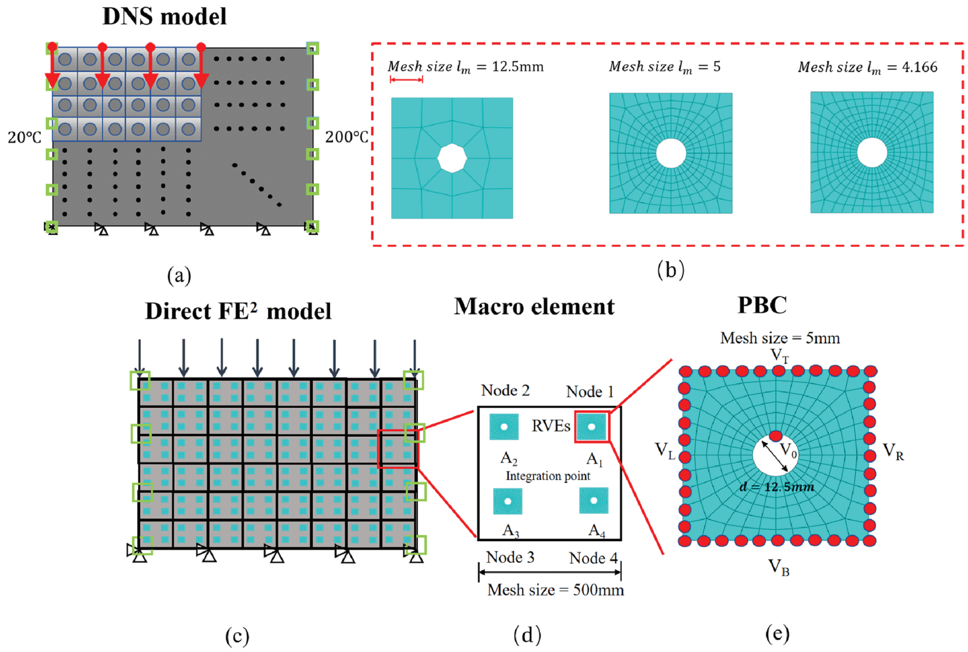

(a) (b)

(c) (d) (e)

Figure 3: Illustration of the perforated steel wall panel and the Direct FE^2 modeling approach. (**a**) Perforated panel with mechanical displacement applied at the top edge and fixed temperatures on the other edges. (**b**) Direct FE^2 model configurations with varying RVE mesh resolutions. (**c**) Macro-scale mesh consisting of 8 × 6 elements; the RVE thickness is scaled 25 times in accordance with Eq. (6). (**d**) Embedding of RVEs at each Gauss integration point of the macro elements. (**e**) Enforcement of PBCs on the RVE domain

Table 1: Material properties of Q335 steel

Parameters	Units	Value
Density ρ	kg/m^3	7850
Elasticity modulus E	GPa	210
Poisson's ratio ν	–	0.3
Conductivity λ	W/(m·K)	50
Expansion α	1/°C	1.2×10^{-5}
Yield stress σ (MPa)		Plastic strain
362		0
373		0.04702
383		0.07514
394		0.10248
401		0.12031
408		0.13782

The accuracy of the Direct FE^2 method is affected by both the macroscopic mesh density and the discretization level of the RVE. To evaluate the influence of RVE mesh size, the macroscopic mesh is initially fixed with $N_L = 8$ in the horizontal direction and $N_W = 6$ in the vertical direction, representing the number of elements along each respective axis. The RVE mesh size is then varied among 12.5, 5, and 4.16 mm.

In the Direct FE^2 framework, an RVE is embedded at each Gauss integration point of the macroscopic elements. The thickness of each RVE is scaled according to Eq. (7), and PBC are enforced at the RVE boundaries. In practice, these PBC are implemented through MPC equations, as formulated in Eq. (6). To eliminate rigid body motion, one node is fixed in each RVE. The macroscopic elements are assigned near-zero material properties to ensure that the system energy is entirely governed by the RVEs, which are given the actual material parameters.

Table 2 presents the maximum displacement u_1 in the x_1 direction, maximum von Mises stress, and maximum reaction F_{x_2} in the x_2 direction for different RVE element sizes. The results indicate that when the RVE element size is less than or equal to 5 mm, the variation in key response quantities is less than 3%, and further refinement to 4.16 mm introduces changes below 1%. Therefore, the RVE element size was set to 5 mm for all subsequent simulations.

Table 2: Sensitivity analysis of RVE mesh size

RVE Size (mm)	Max u_1 (mm)	Error (%)	Max von Mises Stress (MPa)	Error (%)	Max F_{x_2} (kN)	Error (%)
12.5	13.75	–	488.64	–	2.4559E7	–
5.00	13.79	0.29	501.32	2.59	2.4565E7	0.02
4.16	13.75	0.15	503.25	0.38	2.4568E7	0.01

Subsequently, the effect of macro-scale mesh density was investigated with the RVE element size fixed at 5 mm. The number of macro-scale elements was varied from 4 × 3 to 16 × 12, and the corresponding variations in the maximum displacement u_1 in the x_1 direction, maximum von Mises stress, and maximum reaction F_{x_2} in the x_2 direction are listed in Table 3. It can be observed that when the macro mesh is refined to 8 × 6, the variations in all monitored responses are smaller than 1%, and further refinement yields negligible improvements. Thus, a macro-scale mesh of 8 × 6 was selected.

Table 3: Sensitivity analysis of macro-scale mesh density

Macro grid	Max u_1 (mm)	Error (%)	Max von mises stress (MPa)	Error (%)	Max reaction F_{x_2} (kN)	Error (%)
4 × 3	13.75	–	497.65	–	2.4518E7	–
8 × 6	13.78	0.29	501.32	0.74	2.4565E7	0.19
16 × 12	13.80	0.07	501.52	0.04	2.4569E7	0.02

The overall convergence behavior is further illustrated in Fig. 4, where the force-displacement curves corresponding to different mesh configurations are compared. It is evident that the curve obtained with a macro mesh of 8 × 6 and an RVE element size of 5 mm nearly coincides with those of finer meshes. Based on both the tabulated convergence data and graphical comparisons, this mesh configuration was considered to achieve sufficient numerical accuracy while maintaining computational efficiency. Hence, to achieve a balance between computational efficiency and solution accuracy, a macroscopic mesh of 8 × 6 elements is adopted, with each RVE discretized using a structured mesh of 196 CPS4T elements. For comparison, the full DNS model employs a much finer macroscopic discretization of 80 × 60 elements (i.e., RVEs), leading to a substantially larger total element count.

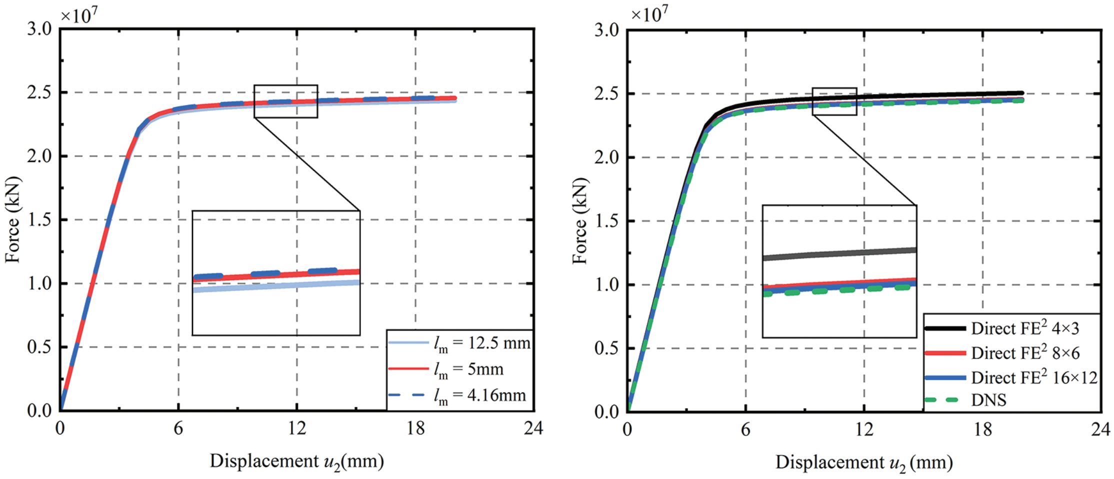

(a) **(b)**

Figure 4: Influence of macro and mesoscale mesh sizes on nodal stress in Direct FE^2 models: (**a**) Simulation results with different mesoscale RVE unit sizes; (**b**) Simulation results with different macroscale RVE unit sizes

Fig. 5 illustrates the distributions of Mises stress, displacements u_1 and u_2, in-plane principal strain, and thermal strain obtained from both DNS and Direct FE^2 simulations. Comparative analyses are conducted at two representative macroscopic locations, denoted as E (1875, 1375) and F (1875, 1375), situated near the upper-left and lower-right corners of the steel plate, respectively. The results indicate a high degree of agreement between the DNS and Direct FE^2 simulations. At the RVE scale, the displacement, stress, and temperature distributions show excellent correlation, with the maximum discrepancy not exceeding 3.8%, thereby validating the reliability and accuracy of the proposed approach. These results confirm that the Direct FE^2 method consistently captures both thermal and mechanical fields, accurately representing the coupled response across scales.

The present validation is carried out against DNS, which provide a highly accurate numerical benchmark. However, it should be acknowledged that this approach lacks direct experimental correlation, thereby limiting the assessment of model performance under real physical conditions. Material imperfections, thermal boundary fluctuations, and microstructural heterogeneity may lead to deviations when compared to laboratory tests. While experimental validation is beyond the scope of this work, the present results can be regarded as a numerical benchmark study. Moreover, previous experimental investigations on the thermo-mechanical behavior of structural steels [50,51] indicate deformation and response evolutions that are in agreement with the trends observed in this study, thereby supporting the reliability of the proposed approach.

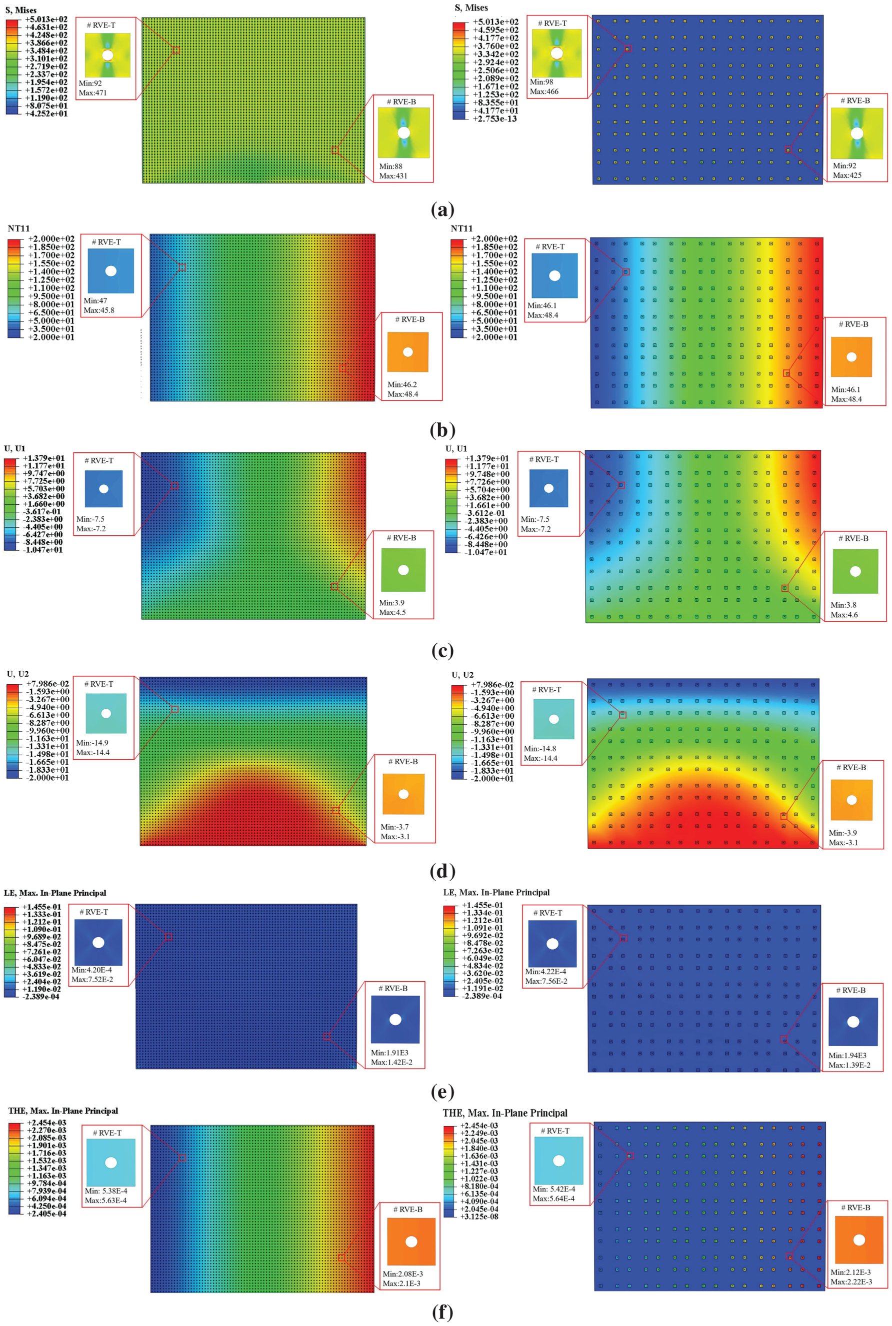

Figure 5: Von Mises stress, displacement u_1, displacement u_2, Max in plane principal strain, and thermal strain at points E ([−1875, 1375]) and F ([1875, −1375]) for the selected RVE with compression displacement $u_c = 20$ mm: (**a**) Mises stress obtained from DNS and Direct FE^2; (**b**) Temperature obtained from DNS and Direct FE^2; (**c**) The displacement u_1 obtained from DNS and Direct FE^2; (**d**) The displacement u_2 obtained from DNS and Direct FE^2; (**e**) Max in plant principal obtained from DNS and Direct FE^2; (**f**) Thermal stain obtained from DNS and Direct FE^2

Finally, to assess computational efficiency, the simulation times of the DNS and Direct FE^2 approaches are compared. All simulations were performed on the same hardware: an Intel Core i9-10900X processor (20 cores, 3.70 GHz) with 64 GB of RAM, with each simulation parallelized across four CPU cores. Total run times were recorded from the ABAQUS job logs. For the perforated panel case, the Direct FE^2 method completed the simulation in 28 s, whereas the DNS approach required 523 s, corresponding to an approximately 19-fold improvement in computational efficiency. This combination of high fidelity and efficiency renders the Direct FE^2 method particularly suitable for generating large sample sets for accurate PCE construction and comprehensive multiscale parametric analyses.

3.2 Results and Discussion of the Multiscale Parametric Study

This section analyzes the impact of material parameter uncertainty on the thermo-mechanical response of steel partition walls by combining the Direct FE^2 method with PCE. The meso-scale elastic modulus and thermal expansion coefficient are selected as random variables. In this study, they are assumed to follow Gaussian (normal) distributions, which are among the most commonly used representations of material property uncertainties in engineering practice. Nevertheless, other probability distributions can also be employed if required. The adoption of the Gaussian distribution in this work is mainly for the sake of convenience in simulation. The mean values of the elastic modulus and thermal expansion coefficient are 210,000 MPa and 1.25 × 10E-5, respectively, with a standard deviation of 0.2, reflecting the variability considered in the present analysis.

The selection and distribution of these parameters are illustrated in Fig. 6. Under various random sampling conditions, multiscale thermo-mechanical simulations are performed to analyze coupled responses. Response variables, including Von Mises stress, displacements u_1 and u_2, maximum in-plane principal strain, and thermal strain, are extracted at two representative points (Points E and F) for detailed analysis.

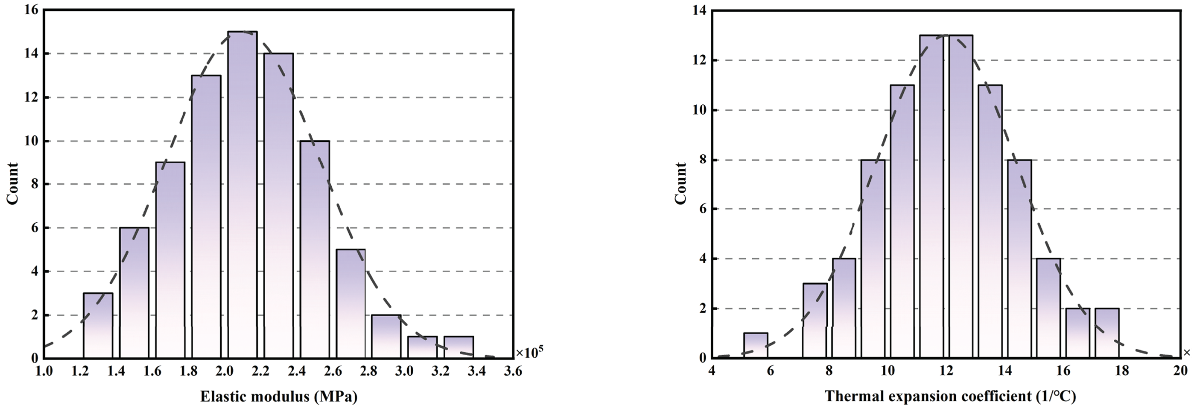

(a) **(b)**

Figure 6: Normal distributions and generated random samples of material parameters for uncertainty analysis: (**a**) Elastic Modulus; (**b**) Thermal Expansion Coefficient

To further quantify the impact of uncertainties on structural responses, PCE is employed to construct surrogate models of orders ranging from first to sixth. The fitting accuracy of these models is evaluated based on the predicted responses, while the CV is used to assess both model precision and sensitivity to input uncertainties across different PCE orders.

3.3 *Single-Variable Uncertainty Analysis*

Tables 4 and 5 present the CV for Von Mises stress, displacements u_1 and u_2, maximum in-plane principal strain, and thermal strain at points E and F as the elastic modulus varies. As the PCE order increases, the CV values decrease steadily, falling well below the commonly adopted 55% threshold in uncertainty analyses. When the PCE order reaches $p = 4$, the differences in CV values become negligible, indicating that this order provides an optimal balance between computational accuracy and efficiency. Consequently, a fourth-order PCE model is considered a reasonable choice for the present study.

Table 4: Impact of PCE expansion order on fitting accuracy at point E (CV%)

Parameter	Order 1	Order 2	Order 3	Order 4	Order 5	Order 6
Von Mises stress	2.11	1.61	0.89	0.39	0.34	0.30
Displacement u_1	0.59	0.35	0.13	0.022	0.020	0.019
Displacement u_2	0.25	0.07	0.018	0.011	0.006	0.005
Max in plane principal	0.02	0.01	0.006	0.004	0.003	0.002
Thermal strain	6.04E-5	6.03E-5	5.98E-5	5.95E-5	5.81E-5	5.80E-5

Table 5: Impact of PCE expansion order on fitting accuracy at point F (CV%)

Parameter	Order 1	Order 2	Order 3	Order 4	Order 5	Order 6
Von Mises stress	1.31	0.33	0.26	0.24	0.21	0.17
Displacement u_1	0.0044	0.00036	0.00023	0.00019	0.00015	0.00014
Displacement u_2	0.0070	0.0040	0.0016	0.00029	0.00025	0.00025
Max in plane principal	0.0054	0.0017	0.0013	0.0010	0.00078	0.00056
Thermal strain	6.04E-5	1.3E-5	1.29E-5	1.28E-5	1.24E-5	1.24E-5

Fig. 7 illustrates the effects of variations in the elastic modulus on structural Von Mises stress, displacements u_1 and u_2, maximum in-plane principal strain, and thermal strain. The stress at points E and F increases with the elastic modulus, reflecting the material's stiffness-higher stiffness results in greater stress under the same mechanical constraints.

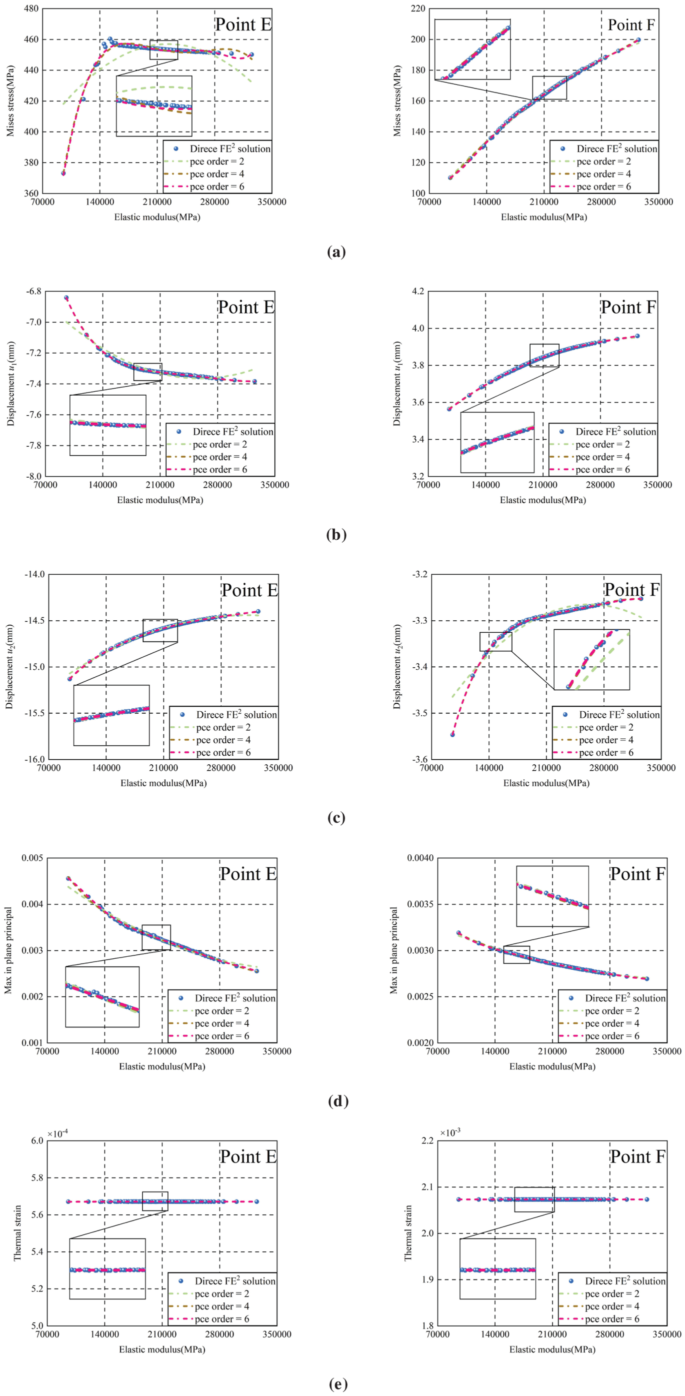

Figure 7: Comparison of original simulation and PCE predictions at points E and F for different polynomial orders (2, 4, and 6) under elastic modulus uncertainty: (**a**) Von Mises stress; (**b**) The displacement u_1; (**c**) The displacement u_2; (**d**) Maximum in-plane principal strain; (**e**) Thermal strain

At point E, the Von Mises stress response exhibits highly nonlinear behavior: it increases with the elastic modulus when the modulus is below approximately 150,000 MPa, then gradually stabilizes or slightly decreases as the modulus continues to rise. In contrast, point F shows a consistently nonlinear increase in Von Mises stress with increasing elastic modulus, suggesting that higher stiffness leads to more complex deformation behavior, potentially due to effects such as material hardening or local yielding.

The displacements u_1 at points E and F display opposing trends with increasing elastic modulus. At point E, located near the constrained and cooler left boundary, thermal expansion is significantly restricted. As the elastic modulus increases, the material becomes stiffer, resulting in stronger resistance to deformation and an amplified leftward displacement caused by reaction forces and thermal stress concentration. Conversely, point F, situated in a hotter and less constrained region, undergoes relatively free expansion. With increasing elastic modulus, the material continues to deform under thermal and mechanical loads, leading to a nonlinearly increasing rightward displacement. These contrasting trends reflect the complex interaction of temperature gradients, boundary conditions, and material stiffness across the structure.

In the x_2-direction, both points E and F exhibit decreasing displacement u_2 with increasing elastic modulus, as stiffer materials have reduced capacity to deform under mechanical loads. The displacement responses at both points also display nonlinear trends, likely arising from local stress concentrations, large deformations, or other nonlinear effects.

The maximum in-plane principal strain at points E and F generally decreases as the elastic modulus increases, consistent with the expectation that stiffer materials undergo less deformation under identical loading conditions. However, the strain response is also nonlinear, likely resulting from complex interactions among mechanical loading, material heterogeneity, and the thermal field.

In contrast, thermal strain exhibits minimal sensitivity to variations in the elastic modulus. As illustrated in the figure, thermal strain at both points remains nearly constant across the range of elastic modulus values, since it is primarily governed by the temperature gradient and the coefficient of thermal expansion, rather than by mechanical stiffness.

Low-order PCE models perform poorly in capturing the complex variations induced by changes in the elastic modulus. Conversely, higher-order PCEs (e.g., fourth- and sixth-order) more effectively represent these nonlinear relationships by accurately approximating the parameter-induced nonlinearities arising from variations in material properties.

Tables 6 and 7 indicate that, under variations in the coefficient of thermal expansion, the CV values at points E and F are considerably smaller than those observed under elastic modulus variations and decrease with increasing PCE order. This is because, under fixed temperature boundary conditions, the influence of the coefficient of thermal expansion on structural response is relatively limited, as thermal strain is predominantly governed by the applied temperature field rather than by moderate variations in the material property itself.

Fig. 8 illustrates the effects of variations in the coefficient of thermal expansion on Von Mises stress, displacement u_1 and u_2, maximum in-plane principal strain and thermal strain.

Under the fixed temperature boundary conditions, as the coefficient of thermal expansion increases,the Von Mises stress at points E and F exhibits distinct trends. At point E, located near the upper displacement-constrained boundary, the stress slightly decreases with increasing thermal expansion coefficient due to partial stress redistribution. In contrast, at point F, situated near the higher-temperature and more constrained boundary, the Von Mises stress exhibits nonlinear behavior, reflecting the combined effects of thermal expansion and the mechanical constraints imposed by the boundary.

Table 6: Impact of PCE expansion order on fitting accuracy at point E (CV%)

Parameter	Order 1	Order 2	Order 3	Order 4	Order 5	Order 6
Von Mises stress	1.42E-4	1.42E-4	1.38E-4	1.37E-4	1.37E-4	1.36E-4
Displacement u_1	2.9E-3	8.8E-4	3.7E-4	1.7E-4	1.2E-4	1.1E-4
Displacement u_2	7.12E-4	7.88E-5	7.02E-5	4.87E-5	4.64E-5	4.49E-5
Max in plane principal	2.73E-3	2.72E-3	2.68E-3	2.67E-3	2.66E-3	2.64E-3
Thermal strain	5.78E-5	5.78E-5	5.51E-5	5.30E-5	4.79E-5	4.75E-5

Table 7: Impact of PCE expansion order on fitting accuracy at point F (CV%)

Parameter	Order 1	Order 2	Order 3	Order 4	Order 5	Order 6
Von Mises stress	1.22E-2	2.9E-2	2.4E-2	1.5E-2	1.5E-2	1.4E-2
Displacement u_1	1.8E-3	8.0E-4	3.2E-4	1.3E-4	1.1E-4	9.69E-5
Displacement u_2	3.2E-3	1.31E-3	6.4E-4	3.0E-4	2.1E-4	1.9E-4
Max in plane principal	3.6E-3	8.3E-4	6.9E-4	4.4E-4	4.3E-4	4.1E-4
Thermal strain	1.51E-5	1.20E-5	1.15E-5	1.12E-5	1.01E-5	1.00E-5

The displacements u_1 at points E and F exhibit direction opposing trends, but with both increasing approximately linearly with the coefficient of thermal expansion. This phenomenon arises primarily from the temperature gradient within the model, where the temperature at the left boundary is 20°C and at the right boundary is 200°C. The thermal expansion at point E, near the low-temperature boundary, is constrained, while the expansion at point F, near the high-temperature boundary, is more free. Additionally, the displacement boundary conditions at the top and the fixed constraints at the bottom further influence the strain distribution, resulting in opposing trends for the horizontal displacements at points E and F.

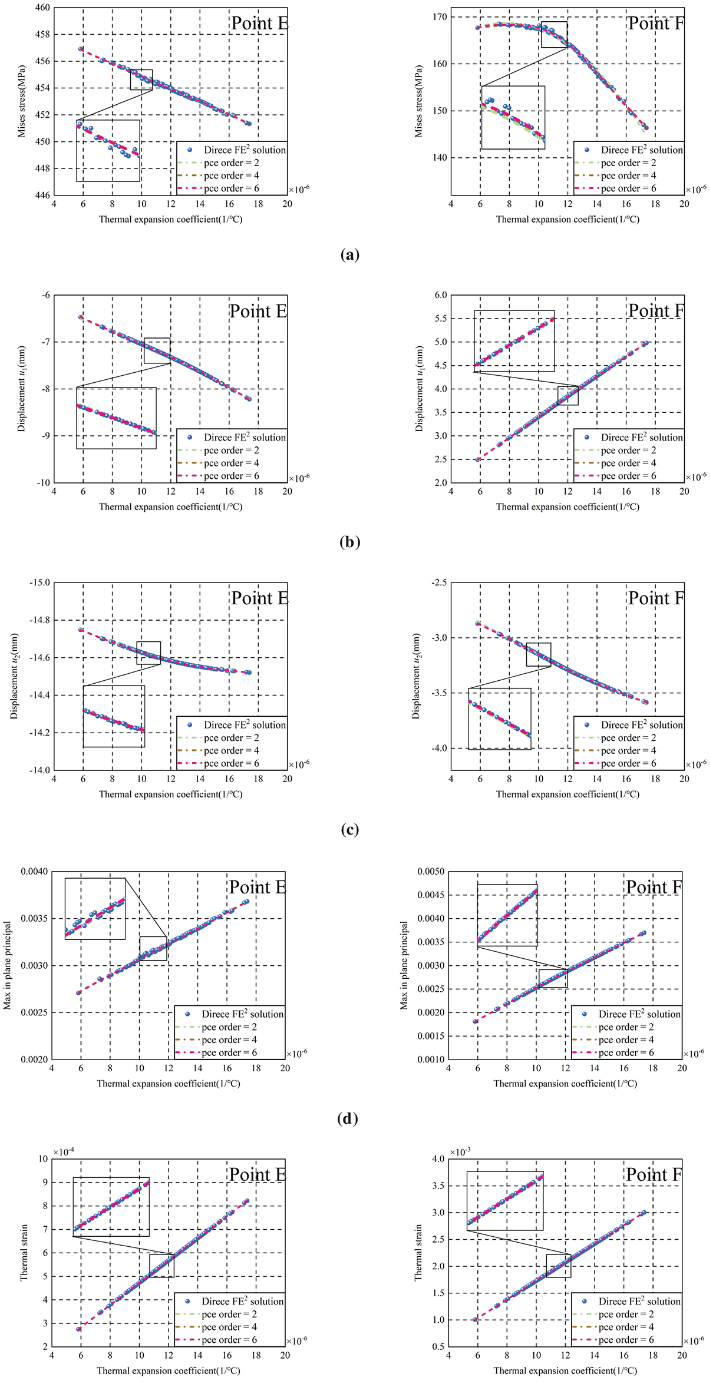

(a)

(b)

(c)

(d)

(e)

Figure 8: Comparison of original simulation and PCE predictions at points E and F for different polynomial orders (2, 4, and 6) under thermal expansion coefficient uncertainty: (**a**) Von Mises stress; (**b**) The displacement u_1; (**c**) The displacement u_2; (**d**) Maximum in-plane principal strain; (**e**) Thermal strain

Similarly, the displacements u_2 increase approximately linearly with the coefficient of thermal expansion at both points, as thermal expansion occurs in the vertical direction and is influenced by the applied boundary conditions.

Furthermore, the maximum in-plane principal strain and thermal strain at both points increase nearly linearly with the coefficient of thermal expansion, as larger β values induce greater thermal deformation under the fixed temperature field.

Low-order PCE models (e.g., second-order) provide a reasonable approximation of these trends; however, higher-order PCEs capture the nonlinear interactions more accurately, especially at locations affected by complex boundary constraints.

3.4 Bivariate-Variable Uncertainty Analysisl Expressions

Based on the univariate analysis results, when the polynomial order $p = 4$, the CV values of the PCE model reach an ideal level. Thus, the bivariate PCE model also adopts an order of $p = 4$. Under this configuration, the CV errors of the five macro-scale responses at point E are 0.0036%, 0.0036%, 0.00008%, 0.004%, and 0.00005%, respectively, while the CV errors for the five macro-scale responses at point F are 0.0022%, 0.0036%, 0.00059%, 0.00082%, and 0.00001%.

Fig. 9 illustrates the combined effects of changes in the elastic modulus and thermal expansion coefficient on structural responses. Both factors simultaneously influence the Von Mises stress at points E and F, with the results aligning with those from the univariate analysis. The displacements u_1 at points E and F show opposing trends, with the thermal expansion coefficient being the dominant factor. As the thermal expansion coefficient increases, the material undergoes more significant expansion or contraction due to the temperature gradient, which leads to opposing displacements at points E and F. The thermal expansion coefficient primarily governs the deformation in the x_1-direction, as it dictates the amount of expansion or contraction caused by temperature changes.

The displacement u_2 at point E is primarily influenced by the variation in the elastic modulus, while the displacement at point F is more sensitive to changes in the thermal expansion coefficient. This can be attributed to the temperature gradient and boundary conditions, with point E being closer to the low-temperature boundary where thermal expansion is more constrained, making the elastic modulus the dominant factor in displacement. In contrast, at point F, which is near the high-temperature boundary, the thermal expansion coefficient plays a more significant role in governing the displacement, as the material undergoes more pronounced thermal expansion in the higher temperature region.

The thermal strain at both points E and F is predominantly controlled by changes in the thermal expansion coefficient, in agreement with theoretical predictions. Thermal strain arises from the material's response to temperature changes, and the thermal expansion coefficient directly determines the amount of expansion or contraction for a given temperature change. Consequently, an increase in the thermal expansion coefficient leads to higher thermal strain at both points, with point F experiencing a more pronounced effect due to the larger temperature difference at that location. These findings highlight the interplay between the elastic modulus and thermal expansion coefficient in shaping the structural response, with the thermal expansion coefficient being the dominant factor in regions exposed to higher temperatures, and the elastic modulus playing a more prominent role in regions with smaller temperature effects.

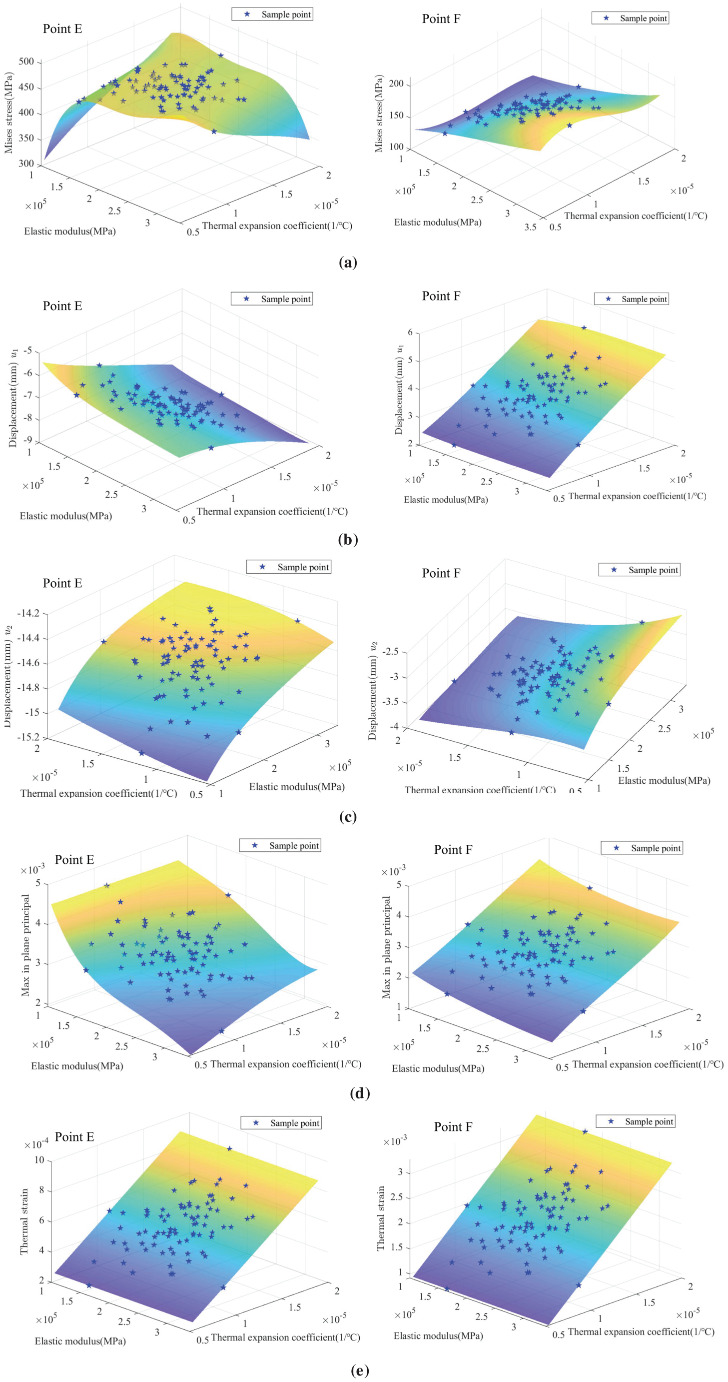

(a)

(b)

(c)

(d)

(e)

Figure 9: Comparison of original simulation and PCE predictions at points E and F for different polynomial orders (2, 4, and 6) under joint uncertainty of elastic modulus and thermal expansion coefficient: (**a**) Von Mises stress; (**b**) The displacement u_1; (**c**) The displacement u_2; (**d**) Maximum in-plane principal strain; (**e**) Thermal strain

4 Conclusions

This study investigated the thermomechanical uncertainty of steel partition walls using the Direct FE^2 method combined with PCE. The primary variables-elastic modulus and coefficient of thermal expansion-were systematically analyzed for their influence on structural responses.

The results indicate that the PCE model with an order of $p = 4$ effectively balances computational efficiency and accuracy. Increasing the PCE order improves the model's ability to capture nonlinear behaviors in Von Mises stress, displacement, Max in plane principal strain, and thermal strain. The elastic modulus primarily affects stress and displacement, while the coefficient of thermal expansion governs thermal strain and deformation, especially under varying temperature gradients. The interaction between these two variables results in complex structural responses, particularly in regions with high thermal gradients.

This work demonstrates the effectiveness of the Direct FE^2-PCE approach in quantifying the thermomechanical uncertainties of steel partition walls. Beyond methodological contributions, the findings provide practical guidance for structural design workflows: the sensitivity of stress and displacement to elastic modulus variations can inform safety factor selection and material quality control, while the dominant influence of thermal expansion on deformation highlights the need for precise thermal property characterization in fire-resistant design. Moreover, the proposed framework enables engineers to efficiently incorporate uncertainty quantification into design optimization and reliability assessments, thus supporting more resilient and cost-effective structural solutions under uncertain thermal and mechanical conditions.

Acknowledgement: The authors gratefully acknowledge Professor Leilei Chen of Huanghuai University, the reviewers, and the members of their research group for their constructive comments and valuable suggestions, which have greatly improved this article.

Funding Statement: This project was supported by the Postgraduate Education Reform and Quality Improvement Project of Henan Province (Grant Nos. YJS2023JD52 and YJS2025GZZ48), the Zhumadian 2023 Major Science and Technology Special Project (Grant No. ZMDSZDZX2023002), the 2025 Henan Province International Science and Technology Cooperation Project (Cultivation Project, Grant No. 252102521011), and the Research Merit-Based Funding Program for Overseas Educated Personnel in Henan Province (Letter of Henan Human Resources and Social Security Office [2025] No. 37).

Author Contributions: The authors confirm contribution to the paper as follows: Conceptualization, Sen Yang and Yanming Xu; Methodology, Sen Yang; Software, Yanming Xu; Validation, Sen Yang, Yanming Xu, and Linchao Liu; Data analysis, Sen Yang; Data curation, Lian Huang; Writing—original draft preparation, Sen Yang; Writing—review and editing, Yanming Xu; Visualization, Sen Yang; Supervision, Linchao Liu. All authors reviewed the results and approved the final version of the manuscript.

Availability of Data and Materials: Data available on request from the authors.

Ethics Approval: Not applicable.

Conflicts of Interest: The authors declare no conflicts of interest to report regarding the present study.

References

1. Wang W-Y, Li G-Q. Fire-resistance study of restrained steel columns with partial damage to fire protection. Fire Saf J. 2009;44(8):1088–94. doi:10.1016/j.firesaf.2009.07.004.
2. Pepper DW, Heinrich JC. The finite element method: basic concepts and applications. Boca Raton, FL, USA: Taylor & Francis; 2005.
3. Szabó B, Babuška I. Finite element analysis: method, verification and validation. Hoboken, NJ, USA: John Wiley & Sons; 2021.
4. Srirekha A, Bashetty K. Infinite to finite: an overview of finite element analysis. Indian J Dent Res. 2010;21(3):425–32.
5. Perrone N, Kao R. A general finite difference method for arbitrary meshes. Comput Struct. 1975;5(1): 45–57. doi:10.1016/0045-7949(75)90018-8.
6. Lipnikov K, Manzini G, Shashkov M. Mimetic finite difference method. J Comput Phys. 2014;257: 1163–227. doi:10.1016/j.jcp.2013.09.038.
7. Eymard R, Gallouët T, Herbin R. Finite volume methods. In: Handbook of numerical analysis. Vol. 7. Amsterdam, The Netherlands: Elsevier; 2000. p. 713–1018.
8. Barth T, Herbin R, Ohlberger M. Finite volume methods: foundation and analysis. In: Encyclopedia of computational mechanics. 2nd ed. Chichester, UK: Wiley; 2018. p. 1–60. doi:10.1002/9781119176817.ecm2010.
9. Minkina W, Dudzik S. Infrared thermography: errors and uncertainties. Chippenham, Wiltshire, UK: John Wiley & Sons; 2009.
10. Sutton MA, Orteu JJ, Schreier H. Image correlation for shape, motion and deformation measurements: basic concepts, theory and applications. New York, NY, USA: Springer; 2009.
11. Ezekoye OA. Conduction of heat in solids. In: SFPE handbook of fire protection engineering. Oxford, UK: Springer; 2016. p. 25–52. doi:10.1007/978-1-4939-2565-0_2.
12. Green AE, Lindsay KA. Thermoelasticity. Oxford, UK: Springer; 1972.
13. Bergman TL. Fundamentals of heat and mass transfer. Hoboken, NJ, USA: John Wiley & Sons; 2011.
14. Hughes TJR. The finite element method: linear static and dynamic finite element analysis. Oxford, UK: Courier Corporation; 2003.
15. Concas F, Mineraud J, Lagerspetz E, Varjonen S, Liu X, Puolamäki K, et al. Low-cost outdoor air quality monitoring and sensor calibration: a survey and critical analysis. ACM Trans Sensor Netw. 2021;17(2):1–44. doi:10.1145/3446005.
16. Hurley MJ, Gottuk DT, Hall JR Jr, Harada K, Kuligowski ED, Puchovsky M, et al. SFPE handbook of fire protection engineering. New York, NY, USA: Springer; 2015.
17. Geers MGD, Kouznetsova VG, Brekelmans WAM. Multi-scale computational homogenization: trends and challenges. J Comput Appl Math. 2010;234(7):2175–82. doi:10.1016/j.cam.2009.08.077.
18. Feyel F. Multiscale FE^2 elastoviscoplastic analysis of composite structures. Comput Mater Sci. 1999;16 (1–4):344–54. doi:10.1016/S0927-0256(99)00077-4.
19. Terada K, Kikuchi N. A class of general algorithms for multi-scale analyses of heterogeneous media. Comput Methods Appl Mech Eng. 2001;190(40–41):5427–64. doi:10.1016/S0045-7825(01)00179-7.
20. Miehe C, der Schrö J, Becker M. Computational homogenization analysis in finite elasticity: material and structural instabilities on the micro-and macro-scales of periodic composites and their interaction. Comput Methods Appl Mech Eng. 2002;191(44):4971–5005. doi:10.1016/S0045-7825(02)00391-2.
21. Raju K, Tay T-E, Tan VBC. A review of the FE^2 method for composites. Multiscale Mult Mod. 2021;4:1–24. doi:10.1007/s41939-020-00087-x.
22. Hou TY, Wu X-H. A multiscale finite element method for elliptic problems in composite materials and porous media. J Comput Phys. 1997;134(1):169–89. doi:10.1006/jcph.1997.5682.

23. Tan VBC, Raju K, Lee HP. Direct FE^2 for concurrent multilevel modelling of heterogeneous structures. Comput Methods Appl Mech Eng. 2020;360:112694. doi:10.1016/j.cma.2019.112694.
24. Nezamabadi S, Yvonnet J, Zahrouni H, Potier-Ferry M. A multilevel computational strategy for handling microscopic and macroscopic instabilities. Comput Methods Appl Mech Eng. 2009;198(27–29):2099–110. doi:10.1016/j.cma.2009.02.026.
25. Garcia CE, Prett DM, Morari M. Model predictive control: theory and practice—a survey. Automatica. 1989;25(3):335–48. doi:10.1016/0005-1098(89)90002-2.
26. Bemporad A, Morari M, Dua V, Pistikopoulos EN. The explicit linear quadratic regulator for constrained systems. Automatica. 2002;38(1):3–20. doi:10.1016/S0005-1098(01)00174-1.
27. Li H, Chen L, Zhi G, Meng L, Lian H, Liu Z, et al. A direct FE^2 method for concurrent multilevel modeling of piezoelectric materials and structures. Comput Methods Appl Mech Eng. 2024;420:116696. doi:10.32604/icces.2023.010584.
28. Zhao A, Tan VBC, Li P, Liu K, Hu Z. A reconstruction approach for concurrent multiscale topology optimization based on direct FE^2 method. Mathematics. 2023;11(12):2779. doi:10.3390/math11122779.
29. Zhi J, Raju K, Tay T-E, Tan VBC. Transient multi-scale analysis with micro-inertia effects using direct FE^2 method. Comput Methods Appl Mech Eng. 2021;67(6):1645–60. doi:10.1007/s00466-021-02012-6.
30. Zhi J, Raju K, Tay T-E, Tan VBC. Multiscale analysis of thermal problems in heterogeneous materials with Direct FE^2 method. Int J Numer Meth Eng. 2021;122(24):7482–503. doi:10.1002/nme.6838.
31. Koyanagi J, Kawamoto K, Higuchi R, Tan VBC, Tay T-E. Direct FE^2 for simulating strain-rate dependent compressive failure of cylindrical CFRP. Compos Part C Open Access. 2021;5:100165. doi:10.1016/j.jcomc.2021.100165.
32. Yeoh KM, Poh LH, Tay TE, Tan VBC. Multiscale computational homogenisation of shear-flexible beam elements: a direct FE^2 approach. Comput Methods Appl Mech Eng. 2022;70(5):891–910. doi:10.1007/s00466-022-02187-6.
33. Xu J, Li P, Poh LH, Zhang Y, Tan VBC. Direct FE^2 for concurrent multilevel modeling of heterogeneous thin plate structures. Comput Methods Appl Mech Eng. 2022;392:114658. doi:10.1016/j.tws.2024.112166.
34. Sudret B, Der Kiureghian A. Stochastic finite element methods and reliability: a state-of-the-art report. Berkeley, CA, USA: Department of Civil and Environmental Engineering, University of California; 2000. Report No. UCB/SEMM-2000/08.
35. Staber B, Guilleminot J. Stochastic modeling of a class of stored energy functions for incompressible hyperelastic materials with uncertainties. Comptes Rendus Mécaniquec. 2015;343(9):503–14. doi:10.1016/j.crme.2015.07.008.
36. Su W, Liu X, Xu S, Wang J, Wang Z. Uncertainty for fatigue life of low carbon alloy steel based on improved bootstrap method. Fatigue Fract Eng Mater Struct. 2023;46(10):3858–71. doi:10.1111/ffe.14109.
37. Liu X, Yu X, Tong J, Wang X, Wang X. Mixed uncertainty analysis for dynamic reliability of mechanical structures considering residual strength. Reliab Eng Syst Saf. 2021;209:107472. doi:10.1016/j.ress.2021.107472.
38. Shen X, Du C, Jiang S, Sun L, Chen L. Enhancing deep neural networks for multivariate uncertainty analysis of cracked structures by POD-RBF. Theor Appl Fract Mech. 2023;125:103925. doi:10.1016/j.tafmec.2023.103925.
39. Honda R. Stochastic BEM with spectral approach in elastostatic and elastodynamic problems with geometrical uncertainty. Eng Anal Bound Elem. 2005;29(5):415–27. doi:10.1016/j.enganabound.2005.01.007.
40. Liu WK, Belytschko T, Mani A. Random field finite elements. Int J Numer Meth Eng. 1986;23(10):1831–45. doi:10.1002/nme.1620231004.
41. Chen L, Lian H, Xu Y, Li S, Liu Z, Atroshchenko E, et al. Generalized isogeometric boundary element method for uncertainty analysis of time-harmonic wave propagation in infinite domains. Appl Math Model. 2023;114:360–78. doi:10.1016/j.apm.2022.09.030.

42. Lian H, Li X, Qu Y, Du J, Meng Z, Liu J, et al. Bayesian uncertainty analysis for underwater 3D reconstruction with neural radiance fields. Appl Math Model. 2025;138:115806. doi:10.1016/j.apm.2024.115806.
43. Zhang B-Y, Ni Y-Q. A hybrid sequential sampling strategy for sparse polynomial chaos expansion based on compressive sampling and Bayesian experimental design. Comput Methods Appl Mech Eng. 2021;386:114130. doi:10.1016/j.cma.2021.114130.
44. Wan H-P, Ren W-X, Todd MD. Arbitrary polynomial chaos expansion method for uncertainty quantification and global sensitivity analysis in structural dynamics. Mech Syst Signal Process. 2020;142:106732. doi:10.1016/j.ymssp.2020.106732.
45. Nath K, Dutta A, Hazra B. Iterative polynomial dimensional decomposition approach towards solution of structural mechanics problems with material randomness. Probab Eng Mech. 2021;66:103159. doi:10.1016/j.probengmech.2021.103159.
46. Chen L, Pei Q, Fei Z, Zhou Z, Hu Z. Deep-neural-network-based framework for accelerating uncertainty quantification of a structural–acoustic fully coupled system in a shallow sea. Eng Anal Bound Elem. 2025;171:106112. doi:10.1016/j.enganabound.2024.106112.
47. Pei Q, Li F, Fei Z, Lian H, Yuan X. A DFE^2-SPCE method for multiscale parametric analysis of heterogenous piezoelectric materials and structures. Comput Mater Contin. 2025;83(1):79–96. doi:10.32604/cmc.2025.061741.
48. Chen L, Lian H, Liu C, Li Y, Natarajan S. Sensitivity analysis of transverse electric polarized electromagnetic scattering with isogeometric boundary elements accelerated by a fast multipole method. Appl Math Model. 2025;141:115956. doi:10.1016/j.apm.2025.115956.
49. Chen L, Liu C, Lian H, Gu W. Electromagnetic scattering sensitivity analysis for perfectly conducting objects in TM polarization with isogeometric BEM. Eng Anal Bound Elem. 2025;172:106126. doi:10.1016/j.enganabound.2025.106126.
50. Wang W-Y, Liu B, Kodur V. Effect of temperature on strength and elastic modulus of high-strength steel. J Mater Civ Eng. 2013;25(2):174–82. doi:10.1061/(ASCE)MT.1943-5533.0000600.
51. Li G-Q, Jiang S-C, Yin Y-Z, Chen K, Li M-F. Experimental studies on the properties of constructional steel at elevated temperatures. J Struct Eng. 2003;129(12):1717–21. doi:10.1061/(ASCE)0733-9445(2003)129:.